

Theoretical investigation on the impact of long surface waves on empirical ERS-1/2 scatterometer models

H.-H. ESSEN

Institut für Meereskunde, Universität Hamburg, Troplowitzstr. 7, D-22529 Hamburg, Germany; e-mail: essen@ifm.uni-hamburg.de

(Received 7 August 1997; in final form 5 June 1998)

Abstract. The influence of long ocean waves on the determination of surface winds from the scatterometer of the European remote sensing satellites (ERS-1/2) is investigated theoretically. The scatterometer operates at 5.3 GHz with vertical polarization (VV). Presently operational algorithms for wind retrieval are based on empirical scatterometer models, which describe the normalized radar cross-section σ_0 in terms of wind speed and direction. These models account for both resonant backscattering from small ripples and their modulation by longer surface waves (wind sea). By making use of the composite surface scattering theory, the portion of σ_0 due to long-wave modulation is quantified. The decomposition of σ_0 allows the investigation of two questions (1) Are σ_0 -models derived for the scatterometer applicable for the synthetic aperture radar (SAR)? On ERS-1/2 both measurements are performed by the same instrument. However, the illuminated areas differ considerably. (2) May the presence of swell distort the retrieval of wind direction? Empirical σ_0 -models account for the wind sea but not for swell, which is an occasional phenomenon with a direction independent of the local wind. Under certain conditions, significant influences have been found: (a) underestimation of wind speed with SAR data of up to 20%, and (b) errors in wind direction due to the presence of some 40°.

1. Introduction

Space-borne scatterometers have been used to measure worldwide surface winds over the ocean. The determination of the surface wind vector from the 5.3 GHz scatterometer of the European remote sensing satellites (ERS-1/2) is based on three normalized radar cross-sections σ_0 , viewing a surface element from different azimuth angles. Retrieval algorithms are based on empirical scatterometer models, which describe σ_0 in terms of wind speed and direction, and radar parameters like incidence angles and polarization. Two major physical processes are involved in connecting these quantities, the generation of surface ripples by wind and the scattering of radar signals from these ripples. While there exists no reliable theory for the first process mentioned, the scattering mechanism is relatively well understood. With respect to wind retrieval, the application of scattering theory requires the knowledge of the spectrum of the scattering waves, i.e. again an empirical model of its dependence on wind speed and direction. However, the inclusion of scattering theory has the advantage that influences of parameters other than wind may be investigated. Such parameters are underlying long waves or surface currents.

As generally accepted, microwave backscatter is mainly due to the small ripples at the sea surface (Bragg scattering theory). According to this theory, σ_0 is proportional to the spectral density of the resonant surface waves, with wavelengths of several centimetres, travelling towards or away from the radar. However, wind is always accompanied also by longer waves (wind sea), with wavelengths of several metres, which modulate the radar cross-section. As tuned by in-situ wind data, empirical σ_0 -models account for this modulation. The present investigations are based on the empirical σ_0 -models of Ifremer (1996) and CMOD4 (Stoffelen and Anderson 1997) of the European Space Agency (ESA), both of which are used for operationally determining the surface wind vector. Other models exist with somewhat better performance for special applications, e.g. that of Rufenach (1995). Janssen and Woiceshyn (1992) propose the inclusion of wave age in the σ_0 -model which, in a sensitivity study (Woiceshyn and Janssen 1992) allowed a reduction of the scatter of ERS-1 retrieved winds by some 30%. However, these approaches are not considered. The purpose of the present paper is to investigate the performance of operational σ_0 -models.

Resonant backscatter is determined by the two-dimensional ripple spectrum and a theoretically known transfer function. The influence of long waves on σ_0 is theoretically investigated by means of the composite surface scattering theory as described by Wright (1968). The long waves are approximated by tilted and moving facets, which carry the scattering ripples. A number of papers on radar scattering make use of the composite surface wave model, e.g. Plant (1986), Donelan and Pierson (1987) and Romeiser *et al.* (1997). Based on physical considerations and air-borne radar measurements, these authors derive models of the ripple spectrum. The recent paper of Romeiser *et al.* (1997) contains a detailed survey of the literature on scattering theory, which will not be repeated here.

As much as possible, the present paper relies on the empirical ERS-1/2 σ_0 -models. It was not the aim to develop a new model of the ripple spectrum, but just to estimate the parameters which are needed to calculate the long-wave σ_0 -modulation. As the long-wave spectrum, which determines the modulation, is only known within certain error bounds, the composite surface theory is confined to the dominant processes. The modulation by facet slopes (tilt modulation) explains some variation of the radar cross-section due to the long waves. However, this process is not able to explain the observed upwind/downwind asymmetry of σ_0 . This phenomenon is accounted for by a second term considering the modulation of the short-wave scattering spectrum by the orbital motion of the long waves (hydrodynamic modulation).

The knowledge of the influence of the long-wave modulation on σ_0 allows the estimation of errors in retrieved winds, in cases where the long wave field deviates from an average wind sea. The empirical σ_0 -models have been tuned with wind data from the open sea. In coastal areas, wind sea may be less developed. On the other hand, additional long waves, like swell, may increase the long-wave field. The empirical σ_0 -models refer to an averaging radius of 50 km. When applying to smaller radii, the retrieved winds may be incorrect. This paper investigates the influence of a reduced illumination area and the influence of swell on the wind retrieval.

The active microwave instrument (AMI) of ERS-1/2 performs both scatterometer and synthetic aperture radar (SAR) measurements. For this reason, the empirical σ_0 -models have been used for gathering information on wind speed from SAR images,

e.g. Alpers and Stilke (1996) and Scoon *et al.* (1996). However, the resolution of the scatterometer is about 50 km and a single σ_0 is affected by the full long-wave spectrum, while the SAR resolution is some 15 m and σ_0 is affected only by the short part of the long wave spectrum. It has been found that, under certain conditions, the application of a scatterometer σ_0 -model to SAR data leads to an underestimation of wind speed.

Rufenach (1996) found some evidence that the presence of swell leads to a deviation of scatterometer-retrieved wind directions from the real ones. This effect may be explained by the modulation of the short scattering waves by underlying longer waves. The influences of both the wind sea and swell have to be considered, which additively contribute to σ_0 . Differently to the wind sea, which is locally generated and follows the wind direction (fetch effect), swell arrives from remote areas with directions independent of the local wind and is not accounted for by empirical σ_0 -models. For given wind speed and direction, swell-induced corrections for the three scatterometer antennas are computed and added to the empirical σ_0 (which includes the wind-sea modulation). The corrected σ_0 are used to retrieve a new wind vector. Deviations of wind direction are strongly dependent on the shape of the swell spectrum and the incidence angle of the radar.

It has been found that, for the effects under consideration, tilt modulation is the dominant process. Theoretically, the dependence on the ripple spectrum reduces to a dependence on the second-order derivatives of σ_0 with respect to the facet slopes. These quantities are estimated either by means of the empirical σ_0 -models or the ripple spectrum. Both a simple theoretical model and a measured spectrum are used. Different presentations of the long-wave spectrum exist, which determines the σ_0 -modulation. The sensitivity of the numerical results (the effect of a reduced illumination area and the influence of swell on the wind retrieval) to variations of the second-order derivatives and to the shape of the long-wave spectrum was investigated.

2. Wind scatterometer of ERS-1

The scatterometers of ERS-1/2 operate at 5.3 GHz (C-band) with vertical polarization for both transmitting and receiving. The scatterometer illuminates the sea surface sequentially by radio pulses from three antennas pointing in different azimuthal directions, 45°, 90° and 135° with respect to the satellite track. The ranges of incidence angle at the sea surface are 18–47° for the mid antenna and 25–59° for the forward and backward looking antennas. This geometry allows radar echos to be received from a 500 km wide swath along the satellite track. As the satellite advances, each point within the swath is successively viewed from the three different azimuthal angles. Normalized radar cross-sections are deduced at nodes with 25 km separation, centred within a 50 km × 50 km resolution cell.

The scatterometer measures the normalised radar cross-section σ_0 . The retrieval of wind velocity is based on the dependence of σ_0 on ocean roughness, which itself depends on surface winds. σ_0 is anisotropic with respect to the angle between wind vector and incident radar beam. With the aid of three σ_0 measurements of the same area from different directions, the surface wind vector can be determined in terms of speed and direction. Figure 1 shows the geometry of the three antennas of the ERS-1 scatterometer and defines the wind direction ϕ , which counts clockwise relative to the mid beam of the scatterometer from the illuminated pixel at the sea surface towards the satellite.

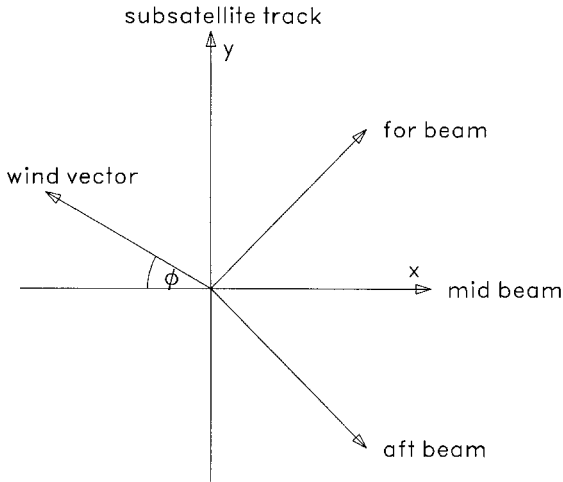


Figure 1. Geometry of the scatterometer antennas and definition of the wind direction ϕ , which is zero with wind blowing antiparallel to the mid beam (towards the satellite).

A number of physical processes affect the retrieval of wind at a certain height (usually 10 m) from measured radar cross-sections. The most important are generation of surface waves by wind, radar backscatter from a rough sea surface, and the structure of the atmosphere between the sea surface and the reference level. The processes are rather complex, and no quantitatively accurate theory based on physical laws exists which includes all the influences mentioned. Instead, the dependence of σ_0 on the wind vector is described by a certain functional dependence, with coefficients tuned by the comparison with in-situ winds. Different approaches exist for the functional dependency as well as for the in-situ data used, buoy-measurements or analysed wind fields. The present analysis makes use of two scatterometer models, that of Ifremer (1996) and CMOD4 of ESA (Stoffelen and Anderson 1997), which both are represented by

$$\sigma_0 = b_0(U, \vartheta) [1 + b_1(U, \vartheta) \cos \phi + b_2(U, \vartheta) \cos(2\phi)]^n \quad (1)$$

where U is the wind speed at 10 m above the sea surface for neutral atmospheric stratification, ϑ the (vertical) incidence angle of the radar beam, and ϕ the wind direction as defined in figure 1. The CMOD4 model ($n=1.6$) was tuned by global wind model data provided by the European Centre of Medium-Range Weather Forecast (ECMWF). Since February 1993, this model has been used by ESA for the determination of the wind vector. The scatterometer model of Ifremer ($n=1.0$) has been tuned by means of buoy data.

For both models, figure 2 displays σ_0 as function of wind direction for different wind speeds and two incidence angles. The models allow the determination of the surface wind vector with an accuracy of speed of 2 ms^{-1} and of direction of 20° , which are the geophysical specifications of the ERS-1/2 scatterometer. The most important difference of both models is the predicted upwind/downwind asymmetry of the radar cross-section, which is quantified by

$$\delta = \frac{\sigma_{\text{up}}}{\sigma_{\text{down}}} - 1 \quad (2)$$

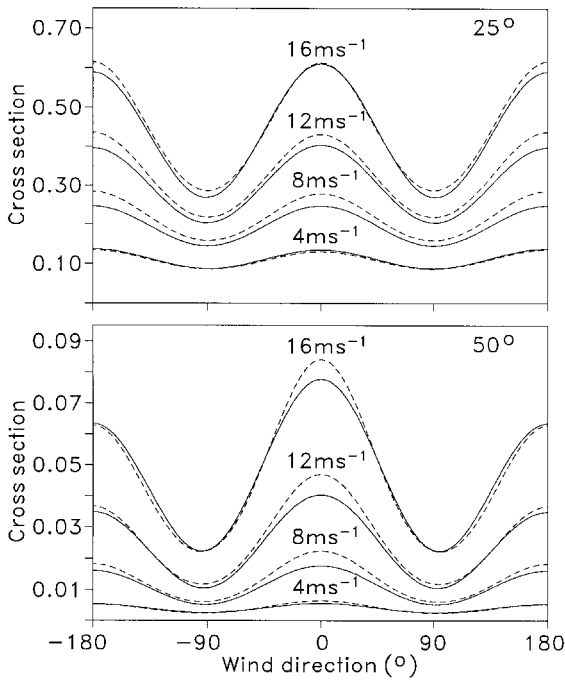


Figure 2. Scatterometer-modd linear σ_0 -values as function of wind direction at different wind speeds U (4, 8, 12, 16 m s^{-1}) and incidence angles ϑ (25° , 50°): solid lines, Ifremer; broken lines, CMOD4.

where $\sigma_{\text{up}} = \sigma_0$ ($\phi = 0^\circ$) and $\sigma_{\text{down}} = \sigma_0$ ($\phi = 180^\circ$). Figure 3 displays δ as function of the incidence angle for different wind speeds and reveals considerable differences between the two scatterometer models.

Wind fields are estimated from the three σ_0 -values by determining all points in the space of wind speed and direction which represent local minima of a specified distance. A maximum-likelihood estimator is applied rather than the least-squares distance, because it gives a measure of the probability that the point lies at this distance from the model solution (Ifremer 1996):

$$e^2 = \sum_{i=1}^3 \frac{(s_{0i} - \sigma_{0i})^2}{(K_i \sigma_{0i})^2} \quad (3)$$

where s_{0i} are the measured and σ_{0i} the modelled radar cross-sections of the three look directions, and K_i are calibration constants provided with the scatterometer data. From the local minima, one solution is selected by making use of the goodness of the fit, continuity of wind directions over the swath, and meteorological background wind fields (ambiguity removal).

3. Composite surface scattering theory

Bragg scattering is the dominant process generating radar backscatter in the range of incidence angles as used by the scatterometer of ERS-1/2, i.e. from 18° to 59° . For smaller incidence angles, specular reflection from tilted surface elements has

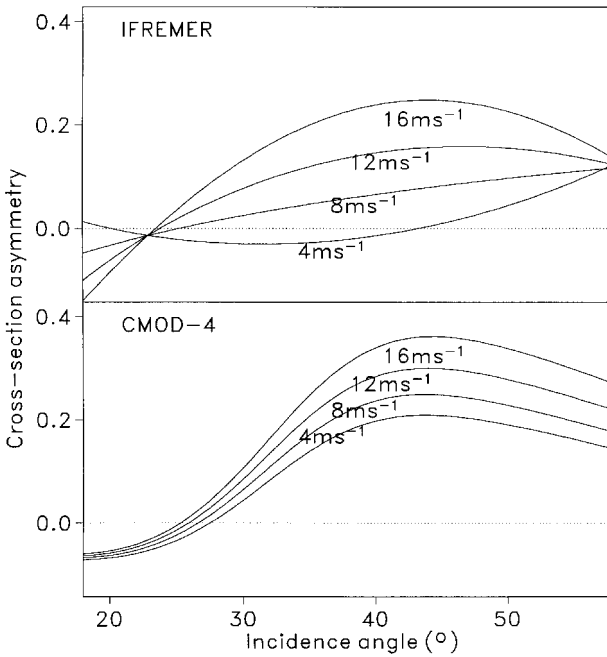


Figure 3. Upwind/downwind asymmetry of the radar cross-section δ (equation 2), as function of incidence angle ϑ at indicated wind speeds U : upper panel, Ifremer; lower panel, CMOD4.

to be taken into account and for larger incidence angles shadowing effects become important. The Bragg condition reads

$$\mathbf{k}_b = \pm 2\mathbf{k}_r, \quad |\mathbf{k}_r| = \frac{\omega}{c} \sin \vartheta \quad (4)$$

where \mathbf{k}_r is the horizontal radar wavevector, ω the circular frequency of the radar, c the speed of light, and ϑ the incidence angle of the radar. \mathbf{k}_b is the vector of surface waves responsible for backscattering. For the scatterometer of ERS-1/2, the range of scattering surface waves extends from 3.3 to 9.2 cm, i.e. in the short-wave range (ripples).

The Bragg scattering theory determines the dependence of σ_0 on the two-dimensional wave-height spectrum by (cf. Wright 1968)

$$\sigma_0 = T(\vartheta)[F(-2\mathbf{k}_r) + F(2\mathbf{k}_r)] \quad (5)$$

with

$$\int F(\mathbf{k}) d\mathbf{k} = \langle \zeta^2 \rangle$$

where ζ is the wave height and the angle brackets denote ensemble averaging. $T(\vartheta)$ is a transfer function and $F(\mathbf{k})$ the two-dimensional waveheight spectrum. Scattering is due to the two resonant wave components travelling parallel and antiparallel to the radar beam. For electromagnetic waves the ocean waves can be treated as frozen.

In order to account for the long surface waves, a composite surface model is

considered. Radar backscatter is due to short ripples on longer waves which locally can be described by tilted facets. The long waves affect the local cross-sections through the variation of the angles of incidence (tilt modulation) and through modulations of the scattering wave spectrum by their orbital motions (hydrodynamic modulation) (cf. Hasselmann 1971):

$$\sigma_0(\mathbf{n}) = T(\vartheta(\mathbf{n}))[\tilde{F}(\mathbf{k}_b(\mathbf{n})) + \tilde{F}'] \tag{6}$$

with

$$\tilde{F}(\mathbf{k}) = F(-\mathbf{k}) + F(\mathbf{k})$$

where $\mathbf{n} = [\partial\zeta/\partial x, \partial\zeta/\partial y]$ is the slope vector, $1/2\tilde{F}$ represents the frozen (symmetric) waveheight spectrum, and \tilde{F}' is the spectral disturbance due to orbital motions, which is assumed to be small. This approach does not account for the slope-dependence of \tilde{F} , which is considered to be a higher-order effect. In addition, Romeiser *et al.* (1997) account for geometric effects. However, because of the high altitude of satellites, these effects are negligible for the present investigations.

Scattering from tilted facets depolarize the received signal. For the application, the slope angles are small and approximated by the slope vector (n_x, n_y) . In the case of vertical polarization of both transmitted and received signal, the formulae of Valenzuela (1978) become

$$T(\vartheta_0; n_x, n_y) = 4\pi \frac{\omega^4 \cos^4 \vartheta}{c^4} \left| \frac{\sin^2(\vartheta_0 - n_x) \cos^2 n_y}{\sin^2 \vartheta} T_{vv} + \frac{\sin^2 n_y}{\sin^2 \vartheta} T_{hh} \right|^2 \tag{7}$$

where the radar beam is assumed to be parallel to the x -axis (mid beam in figure 1). The resultant incidence angle ϑ and the Bragg wavenumber \mathbf{k}_b relative to the facet are

$$\left. \begin{aligned} \vartheta &= \cos^{-1} [\cos(\vartheta_0 - n_x) \cos n_y] \\ \mathbf{k}_b &= 2\mathbf{k}_r \{ \sin(\vartheta_0 - n_x), -\cos(\vartheta_0 - n_x) \sin n_y \} \end{aligned} \right\} \tag{8}$$

where ϑ_0 is the incidence angle at the undisturbed surface. The transfer coefficients are

$$\left. \begin{aligned} T_{vv} &= \frac{(\varepsilon - 1)[\varepsilon(1 + \sin^2 \vartheta) - \sin^2 \vartheta]}{(\varepsilon \cos \vartheta + \sqrt{\varepsilon - \sin^2 \vartheta})^2} \\ T_{hh} &= \frac{\varepsilon - 1}{(\cos \vartheta + \sqrt{\varepsilon - \sin^2 \vartheta})^2} \end{aligned} \right\} \tag{9}$$

where ε is the complex dielectric constant of water.

The wave heights of the modulating long waves may be represented by a Fourier sum:

$$\zeta = \sum_{\mathbf{k}} Z_{\mathbf{k}} \exp \{i(\mathbf{K}\mathbf{x} - \Omega t)\} + c.c. \tag{10}$$

where $Z_{\mathbf{k}}$ is the Fourier amplitude, and the complex conjugate *c.c.* has been added in order to account for real ζ . The modulus of the wave vector \mathbf{K} and the circular frequency Ω are connected by the dispersion relation of deep-water gravity waves, $\Omega^2 = gK$, with g being the acceleration of the earth. The horizontal components of

the slope vector \mathbf{n} and the orbital velocity \mathbf{u} depend on the wave height by

$$\left. \begin{aligned} n_\alpha &= \frac{\partial \zeta}{\partial x_\alpha} \\ \frac{\partial u_\alpha}{\partial t} &= -gn_\alpha \quad (\alpha = x, y) \end{aligned} \right\} \tag{11}$$

The long waves are assumed to be a random homogeneous process with ensemble means:

$$\left. \begin{aligned} \langle Z_{\mathbf{k}} \rangle &= 0 \\ \langle Z_{\mathbf{k}} Z_{\mathbf{k}'} \rangle &= 0 \quad \text{if } Z_{\mathbf{k}} \neq Z_{\mathbf{k}'}^* \end{aligned} \right\} \tag{12}$$

Following Hasselmann (1971), equation (6) is expanded into a Taylor series around the mean slope, which is zero. The mean radar cross-section is obtained by averaging over all facets in the illuminated area, i.e. by taking ensemble means. Accounting for vanishing mean slopes $\langle n_x \rangle = \langle n_y \rangle = 0$, equations (10–12), and for $\partial T / \partial n_y = 0$, as T is an even function of n_y , equation (7), the lowest order corrections become

$$\left. \begin{aligned} \Delta \sigma_0 &= \langle \sigma_0(\mathbf{n}) \rangle - \sigma_0 \\ &= \frac{1}{2} \frac{\partial^2 \sigma_0}{\partial n_\alpha \partial n_\beta} \langle n_\alpha n_\beta \rangle + \frac{\partial T}{\partial n_x} \langle \tilde{F}' n_x \rangle \quad (\alpha, \beta = x, y) \end{aligned} \right\} \tag{13}$$

with summation over double indices.

It is assumed that the spectral disturbance varies in accordance with the long waves:

$$\tilde{F}' = \tilde{F} \sum_{\mathbf{k}} R_{\mathbf{k}} Z_{\mathbf{k}} \exp \{i(\mathbf{Kx} - \Omega t)\} + c.c. \tag{14}$$

where $R_{\mathbf{k}}$ is the modulation transfer coefficient. Equation (11) shows that slopes and orbital motions vary out of phase. With $R_{\mathbf{k}}$ being real, the second term in equation (13) vanishes. However, relaxation introduces a phase delay and in turn a complex $R_{\mathbf{k}}$ and a nonvanishing contribution of the second term. The spectral disturbance \tilde{F}' may be estimated by applying the principle of conservation of action (Alpers and Hasselmann 1978). With the radar beam being parallel to the x -axis ($k_x = k_b, k_y = 0$), the theory yields

$$R_{\mathbf{k}} = - \frac{\Omega}{\Omega + i\mu} \frac{k_b K_x}{K} \left(\frac{K_x}{F} \frac{dF}{dk_x} + \frac{K_y}{F} \frac{dF}{dk_y} - \frac{K_x}{\omega} \frac{d\omega}{dk} \right) \tag{15}$$

where μ is the relaxation rate of the short waves, of which frequency and wavenumber are connected by the dispersion relation

$$\omega^2 = gk + \frac{\tau}{\rho} k^3 \tag{16}$$

where τ is the surface tension and ρ the density of water.

Inserting the slope (equation 11) and the spectral perturbation (equation 14) into equation (13), taking into account the statistical assumptions (equation 12), and

replacing the summation by an integration, one obtains

$$q = \frac{\Delta\sigma_0}{\sigma_0} = \int \left(\frac{K_\alpha K_\beta}{2\sigma_0} \frac{\partial^2 \sigma_0}{\partial n_\alpha \partial n_\beta} - \text{Im}(R_{\mathbf{K}}) \frac{K_x}{T} \frac{\partial T}{\partial n_x} \right) F(\mathbf{K}) d\mathbf{K} \quad (17)$$

with $2\langle Z_{\mathbf{K}} Z_{\mathbf{K}}^* \rangle = F(\mathbf{K}) d\mathbf{K}$. The second term (hydrodynamic modulation) changes sign in the case of a reversal of the wind-driven sea and thus introduces an upwind/downwind asymmetry of $\Delta\sigma_0$.

4. Numerical results

As winds are always accompanied by wind waves, empirical scatterometer models contain a portion due to the modulation of the (long) wind sea. Equation (17) accounts for two processes, tilt and hydrodynamic modulation. Tilt modulation will be found to be the dominant process and is discussed at first. Tilt modulation, first term of equation (17), depends on the second-order derivatives of σ_0 with respect to the facet slopes and the two-dimensional long-wave spectrum. In principle, the derivatives can be estimated from the empirical scatterometer model (equation 1), with equation (8) determining the slope-induced deviations of the incidence angle and the wind direction with respect to radar beam. However, the theory is based on the undisturbed short-wave spectrum, while the empirical scatterometer model includes the modulation by the wind sea. For this reason, the second-order derivatives are also computed by means of the theoretical equations (6–9). This approach requires the knowledge of the undisturbed short-wave spectrum, which also is needed for the estimating the influence of hydrodynamic modulation, the second term in equation (17).

The two-dimensional wavenumber spectrum of ocean waves is represented as

$$F(\mathbf{k}) = \frac{1}{k} E(k) S(\varphi) \quad (18)$$

with

$$\int E(k) dk = \langle \zeta^2 \rangle$$

$$\int S(\varphi) d\varphi = 1$$

where $\mathbf{k} = (-k \cos \varphi, k \sin \varphi)$ is the wave vector and φ counts in accordance with the wind direction ϕ (figure 1).

Based on the empirical σ_0 -models, a model short-wave spectrum has been derived. The aim is to reasonably reproduce the empirical σ_0 -models. The attempt of constructing an appropriate spectrum based on non-dimensional parameters was not successful. The present model spectrum adopts the dependence on wind speed of the spectrum of Romeiser *et al.* (1997), which has been deduced from air-borne σ_0 -measurements within the frequency range from 1 to 34 GHz and covers the wavelengths of both the small scattering ripples and the long modulating wind waves. For the application in the short-wave range, a simplified approach with respect to the wavenumber dependence is used:

$$E(k) = \frac{A_k}{k^3} \left(\frac{k_N}{k} \right)^2 \left(\frac{U}{U_0} \right)^\alpha \quad (19)$$

with

$$A_k = 0.0038$$

$$k_N = 90 \text{ rad m}^{-1}$$

$$U_0 = 1 \text{ m s}^{-1}$$

$$\alpha = 0.6 + 0.54 \frac{k}{k_N}$$

where the arbitrary normalisation k_N has been chosen to be about the Bragg wavenumber at an incidence angle of $\vartheta = 25^\circ$. Romeiser *et al.* (1997) consider a Gaussian function for the angular distribution. However, the empirical models are based on a \cos^2 -dependence, which is adopted here:

$$S(\varphi) = \frac{1}{2\pi} \left[1 + A_\varphi U \left(\frac{k}{k_N} \right)^2 \cos(2(\phi - \varphi)) \right] \quad (20)$$

with

$$A_\varphi = 0.008$$

where ϕ is the wind direction and φ the azimuthal angle of the radar beam, e.g. $\varphi = 0$ for the mid beam (figure 1). The angular function refers to the frozen spectrum and accounts for a dependence on both wind speed and wavenumber, as suggested by the empirical σ_0 -models (figure 2).

With a wave staff, Stolte (1990) measured short-wave spectra at a research tower in the North Sea. The frequency spectrum, which he derived by fitting a model spectrum to his data, is valid for wind speeds of up to some 8 m s^{-1} . Transformation into a wavenumber spectrum yields

$$E(k) = \frac{\alpha g^2}{(2\pi)^5} \frac{d\omega}{dk} \left(\frac{W}{2\pi} \right)^{-n} \quad (21)$$

with

$$n = 5.00 - 0.122 U + 0.00391 U^2$$

$$\log \alpha = -2.87 + 0.273 U - 0.0153 U^2$$

The circular frequency ω depends on the wavenumber k by the dispersion relation (equation 16).

Figure 4 compares model spectra (equation 19), and measured spectra (equation 21) at different wind speeds. The model spectrum reveals a stronger decrease with increasing wavenumber than the measured one. The dependence on wind of the measured spectrum is even higher than that of the model spectrum.

The dielectric constant of water ε varies with the radar frequency and depends on the salinity and temperature. At 5.3 GHz the value for sea water of 20°C is (Ulaby *et al.* 1986)

$$\varepsilon = 68 - 32i \quad (22)$$

Variations of ε due to changes in salinity or temperature have no remarkable influence on the numerical results.

Figure 5 compares second-order σ_0 -derivatives as derived from an empirical σ_0 -model (empirical approach) and by means of the theoretical transfer function in

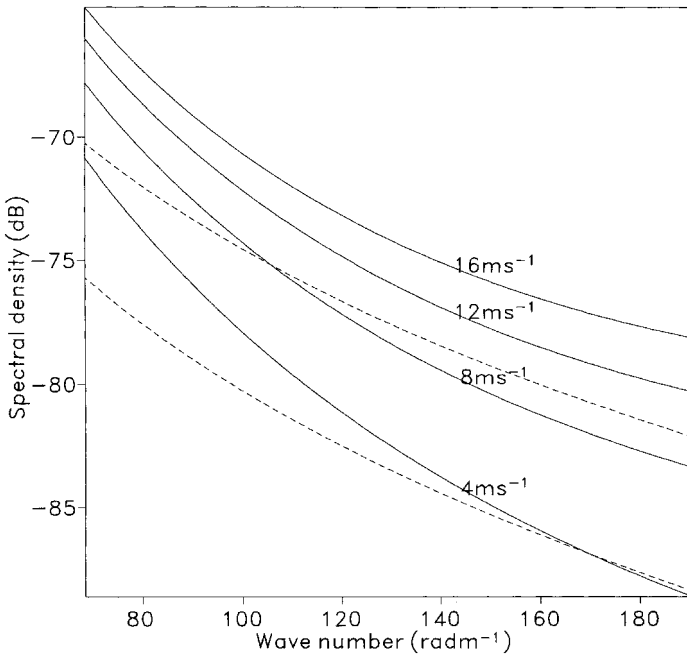


Figure 4. One-dimensional short-wave spectra $E(k)$ (equation 18) for the wavenumber range covered by the scatterometer of ERS-1/2: full lines, model spectrum (equation 19) at indicated wind speeds U ; dashed lines, spectrum retrieved from measurements of Stolte (1990) (equation 21) at wind speeds of 4 and 8 m s^{-1} , respectively.

connection with short-wave spectra (theoretical approach). Both the model and the measured short-wave spectrum (equations 19 and 21), are used with the angular distribution of equation (20). Two incidence angles are considered; the results refer to a wind speed of 8 m s^{-1} . The discrepancies between both approaches can be attributed partly to the fact that the empirical σ_0 -model includes the modulation by the wind sea and partly to the different parametrizations of the models. For example, the strong variation of the empirical $\partial\sigma_0^2/\partial n_x^2$ with wind direction is due to the dependence of b_2 in equation (1) on the incidence angle ϑ .

Figure 5 reveals that $\partial\sigma_0^2/\partial n_x^2$ dominates and is positive, while the other derivatives are either negative or change sign. Both empirical and theoretical σ_0 -derivatives show a strong dependence on the incidence angle ϑ of the radar. From this finding it may be expected that the importance of tilt modulation decreases with increasing incidence angle. It should be mentioned that these results are independent of wind speed and the empirical model used, i.e. that of Ifremer or CMOD4. Generally, it can be concluded that the dominating $\partial\sigma_0^2/\partial n_x^2$ is overestimated by the empirical approach, while the theoretical approach yields smaller values with the measured spectrum than with the model spectrum.

The modulation of σ_0 by long waves depends on the two-dimensional wavenumber spectrum of the long waves which, as that of the short waves, is decomposed into the one-dimensional wavenumber spectrum and the angular distribution (cf. equation 18). Capital letters (wavenumber K and circular frequency Ω) are used for distinguishing short and long waves. Different spectra from the literature are discussed with respect to their influence on the σ_0 -modulation. The wavenumber spectra

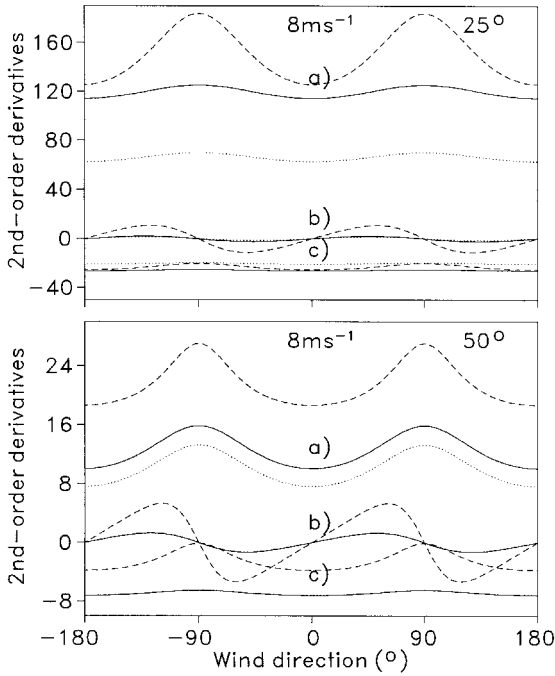


Figure 5. Second-order derivatives of σ_0 with respect to the facet slopes at a fixed wind speed U (8 m s^{-1}) and two incidence angles β , 25° (upper panel) and 50° (lower panel), derived from the Ifremer scatterometer model (dashed lines) and by means of Bragg theory with the model spectrum (full lines) and with the measured spectrum (dotted lines) of equations (19) and (21), respectively: (a) $\sigma_0^{-1} \partial^2 \sigma_0 / \partial n_x^2$; (b) $\sigma_0^{-1} \partial^2 \sigma_0 / \partial n_x \partial n_y$; (c) $\sigma_0^{-1} \partial^2 \sigma_0 / \partial n_y^2$.

under consideration can be represented as

$$E(K) = \frac{A}{K^3} \exp \left[-\alpha \left(\frac{\Omega}{\Omega_p} \right)^{-4} \right] e(\Omega) \tag{23}$$

with

$$e(\Omega) = \gamma^\beta, \quad \beta = \exp \left[-0.5 \left(\frac{\Omega - \Omega_p}{s\Omega_p} \right)^2 \right]$$

where Ω_p is the peak frequency of the frequency spectrum, which usually is derived from time series of wave-height measurements.

Pierson and Moskowitz (1964) proposed a spectrum for a fully developed sea:

$$\left. \begin{aligned} A &= 0.005 \\ \Omega_p &= 0.88 \frac{g}{U} \\ \alpha &= 1.25 \\ e(\Omega) &= 1 \end{aligned} \right\} \tag{24}$$

Based on measurements during JONSWAP (Joint North Sea Wave Project)

Hasselmann *et al.* (1973) modified the Pierson–Moskowitz spectrum by describing both the amplitude A and peak frequency Ω_p in equation (23) in terms of a non-dimensional fetch and by introducing the peak enhancement function $e(\Omega)$. A typical JONSWAP spectrum is given by

$$\begin{aligned}
 A &= 0.038\bar{x} & \Omega_p &= \frac{22g}{U}\bar{x}^{-0.33} & \text{with } \bar{x} &= \frac{gx}{U^2} \\
 \alpha &= 1.25 & \gamma &= 3.0 & s &= \begin{cases} 0.08 & \text{if } \Omega \leq \Omega_p \\ 0.12 & \text{if } \Omega > \Omega_p \end{cases}
 \end{aligned} \tag{25}$$

where \bar{x} is the non-dimensional fetch and x the fetch measured in metres.

A somewhat different spectrum has been deduced from measurements in the Lake Ontario by Donelan *et al.* (1985). Instead of the non-dimensional fetch, the ratio of wind speed to the phase velocity of the peak frequency is used for parametrization:

$$\begin{aligned}
 A &= 0.003 \frac{\Omega}{\Omega_p} \bar{u}^{0.55} & \text{with } \bar{u} &= \frac{U}{V_p} \\
 \alpha &= 1 & \gamma &= \begin{cases} 1.7 & \text{if } \bar{u} \leq 1 \\ 1.7 + 6.0 \log(\bar{u}) & \text{if } \bar{u} > 1 \end{cases} & s &= 0.08(1 + 4\bar{u}^{-3})
 \end{aligned} \tag{26}$$

where V_p is the phase velocity at the peak frequency Ω_p .

Figure 6 displays wavenumber spectra of the waveheight, $E(K)$, and waveslope, $K^2 E(K)$, for a wind speed of 8 m s^{-1} and different fetches. Linear scales have been chosen in order to clarify the differences of variances. The long fetch ($\bar{x} = 2 \times 10^4$, $\bar{u} = 0.84$) refers to a fully developed sea. The peak wavenumbers of both JONSWAP and Donelan spectrum coincide with that of the Pierson–Moskowitz spectrum. Decreasing the fetch by a factor of 10 and adopting the JONSWAP peak frequency for the Donelan spectrum ($\bar{x} = 2 \times 10^3$, $\bar{u} = 1.8$), the waveheight spectra contain considerably less variance. Their peaks are hardly visible in the upper panel of figure 6.

However, the σ_0 -modulation depends on the waveslope spectrum (cf. equation 17), which is displayed in the lower panel of figure 6 for wavelengths longer than 6.3 m. The integration in equation (17) extends to a shorter cutoff wavelength, which in accordance with the composite wave model should be large compared to the Bragg scattering waves, e.g. 0.5 m. The total variance of the slopes is found to be nearly independent of the fetch for the JONSWAP spectrum and to be about the same as that of the Pierson–Moskowitz spectrum. Dividing or multiplying the cutoff wavelength by a factor of 2 increases or decreases the variance by some 25%. These results are independent of wind speed.

Due to the less steep falloff at high wavenumbers, the Donelan spectrum yields deviating slope variances. Considering a cutoff wavelength of 0.5 m, the variance of the short-fetch spectrum is about the same at 4 m s^{-1} wind speed and by a factor of 2 higher at 16 m s^{-1} than that of the Pierson–Moskowitz spectrum. With increasing wind speed the long-fetch spectrum contains between 100 and 50% more variance than the short-fetch spectrum. Dividing or multiplying the cutoff wavelength by a factor of 2 increases or decreases the variance by some 50%. It should be mentioned that the cutoff wavenumbers used exceed the bound for which the Donelan spectrum has been proved ($\Omega < 3.5\Omega_p$).

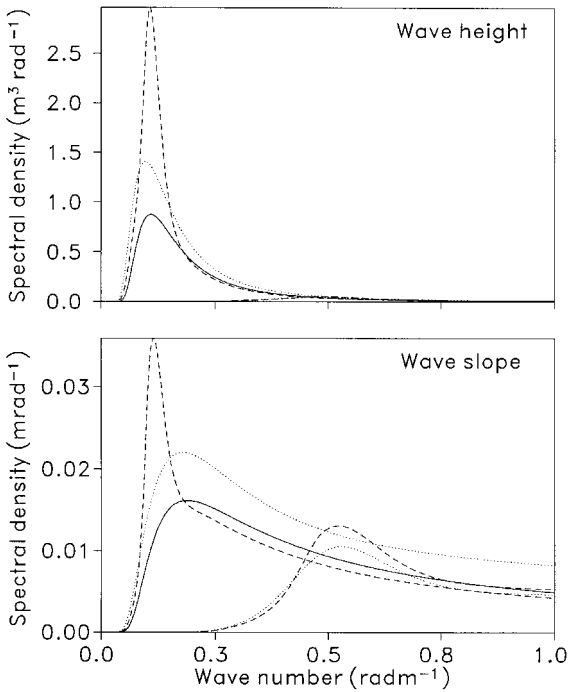


Figure 6. Long-wave spectra of wave-height $E(K)$ (upper panel) and wave-slope $K^2E(K)$ (lower panel), Pierson–Moskowitz (full lines), JONSWAP (dashed lines), Donelan (dotted lines) (cf. equations 23–26). The latter two spectra are displayed for long and short fetch, respectively.

The directional distribution is assumed to be

$$S_w(\varphi) = \begin{cases} 0.64 \cos^2(\varphi - \phi) & \text{if } |\varphi - \phi| \leq 90^\circ \\ 0 & \text{otherwise} \end{cases} \quad (27)$$

and follows the wind direction. In addition, computations have been carried out with a \cos^4 -distribution. The results are similar and not presented here.

The dashed lines in figure 7 display the theoretical σ_0 as computed by means of equation (5) with transfer function (equation 7) and short-wave spectrum (equations 18–20). It does not account for the modulation by long waves. The full lines represent σ_0 -values accounting for the tilt modulation. The computations have been carried out with a Pierson–Moskowitz spectrum and a cutoff wavenumber of 0.5 m. Independent of fetch the JONSWAP spectrum yields about the same result. For comparison, the σ_0 -values of the Ifremer model are presented (dotted lines). In order to account for tilt modulation only, the non-symmetric term is omitted, i.e. $\cos \phi \equiv 1$ in equation (1). Figure 7 confirms that the impact of tilt modulation strongly decreases with increasing incidence angle.

The hydrodynamic modulation, the second term of equation (17), causes the upwind/downwind asymmetry of σ_0 . The predictions of the scatterometer models of Ifremer and CMOD4 differ considerably (figure 3). For theoretically estimating the contribution of the hydrodynamic modulation the derivation of the transfer function with respect to the facet slope is needed, which may not be determined from an

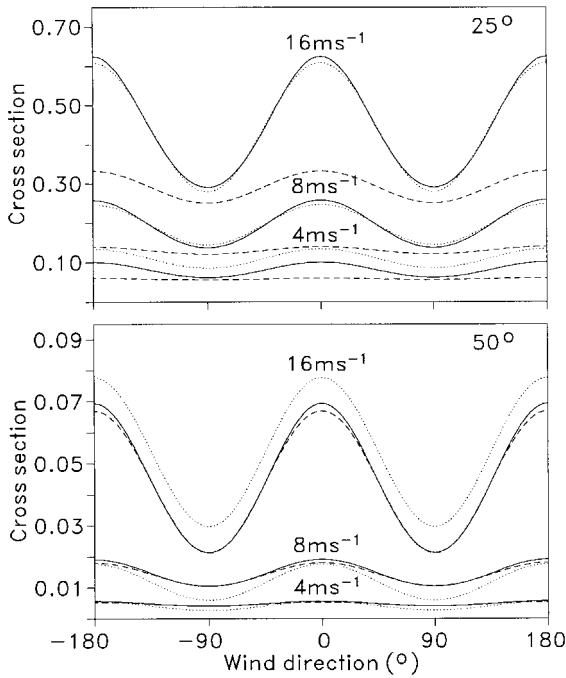


Figure 7. Influence of tilt modulation. Dashed lines represent theoretical σ_0 without wind-sea modulation, full lines account for tilt-modulation, and dotted lines represent the symmetric portion of the Ifremer model. The radar cross-sections are displayed in terms of wind direction for selected wind speeds U (4, 8, 16 m s^{-1}) and incidence angles β , 25° (upper panel) and 50° (lower panel).

empirical σ_0 -model and is derived from equation (7). By making use of the modulation transfer coefficient (equation 15) and realistic relaxation rates, e.g. of those of Hughes (1978), it is not possible to reproduce the high values of δ in figure 3. Possible reasons for this shortcoming are the neglect of higher than second order terms of the Taylor expansion of equation (6), or the simplifications used in deriving R_k , (equation 15) by means of the principle of conservation of action. From observations obtained with an air-borne real-aperture C-band radar at vv polarization, Hauser and Caudal (1997) concluded that, for incidence angles around 34°, the hydrodynamic modulation is underestimated by theoretical approaches.

It is not the purpose of the present investigations to derive an accurate theory for the hydrodynamic modulation. For this reason, the authors chose an approach, instead of equation (15), which allows one to reasonably reproduce the σ_0 -curves of figure 3. The dependence of the coefficient R_k on the long waves from equation (15) was adopted, but the dependence on the Bragg wavenumber was changed:

$$\text{Im}(R_k) = -\frac{K_x^2}{K} \left(\frac{k}{k_N} \right)^{2.5} \quad (28)$$

Like the tilt modulation, the hydrodynamic modulation is determined by the variance of slopes.

Figure 8 (full lines) displays computed σ_0 -values accounting for both tilt and hydrodynamic modulation. The dashed lines reproduce figure 7, i.e. account for tilt

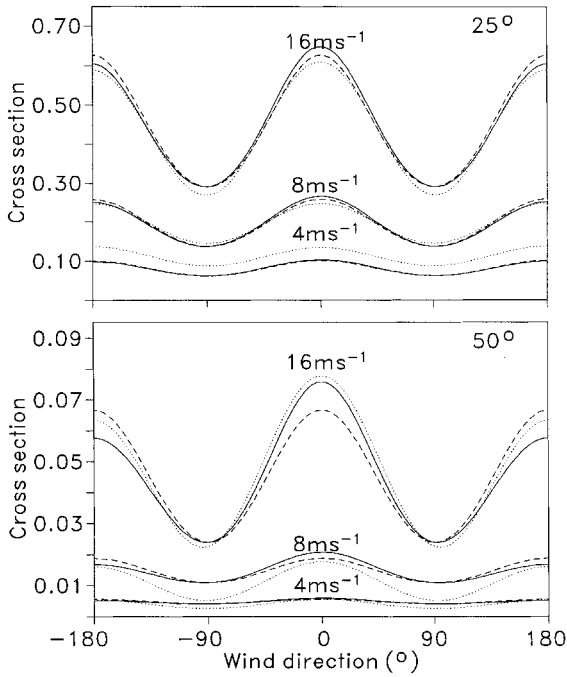


Figure 8. Influence of hydrodynamic modulation. Dashed lines represent theoretical σ_0 accounting for tilt modulation (full lines in figure 7), full lines for both tilt and hydrodynamic modulation, and dotted lines represent the Ifremer model. The radar cross-sections are displayed in terms of wind direction for selected wind speeds U (4, 8, 16 ms^{-1}) and incidence angles ϑ , 25° (upper panel) and 50° (lower panel).

modulation only. For comparison, the Ifremer σ_0 -model is plotted (dotted lines). Deviating from figure 7, the full non-symmetric model is displayed. It can be stated that there is reasonable agreement between the computed σ_0 -values and the Ifremer model. Somewhat better fits should be possible by modifying either the short-wave or the long-wave spectrum. However, the influence of improved models to the applications, presented in the following, are small.

Figure 9 (full lines) displays the upwind/downwind asymmetry δ of σ_0 (equation 2), computed analogously to figure 8. The comparison with figure 3 reveals strong differences. Changes of sign occur at small incidence angles ($\approx 25^\circ$) for the empirical δ and at a large incidence angle (57°) for the theoretical δ . The latter zero crossing is due to $\partial T/\partial n_x$, entering into equation (17) and shown as dashed line in figure 9. From this disagreement it may be concluded that higher order terms in addition to those of equation (6) might be of importance. However, the following investigations reveal that for incidence angles smaller than some 30° the tilt modulation dominates the hydrodynamic modulation. Within the interval of incidence angles between 30° and 50° , the present approach reasonably describes the empirical upwind/downwind asymmetry of σ_0 .

4.1. Applicability of scatterometer models to SAR

The SAR on ERS-1/2 operates at the same frequency and polarization as the scatterometer. The incidence angles 20–26° are within the scatterometer range, i.e. it may be concluded that the scatterometer σ_0 -models can be applied for retrieving

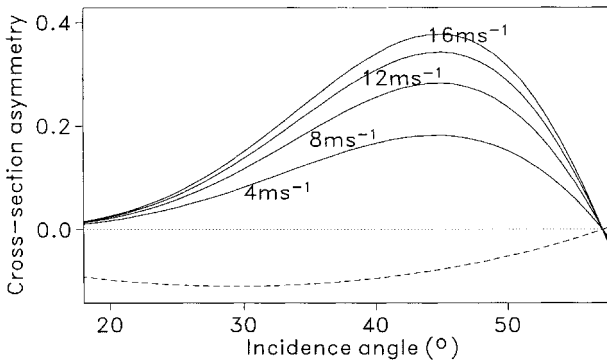


Figure 9. Theoretical upwind/downwind asymmetry of the radar cross-section δ (equation 2), in terms of the incidence angle θ for indicated wind speeds U (full lines), and derivation of the transfer function $T^{-1}\partial T/\partial n_x$, multiplied by a factor of 0.1 (dashed line).

the wind speed from SAR images. It should be mentioned that this is only possible if the wind direction is known. However, the resolution of the scatterometer is about 50 km and a single σ_0 is affected by the full long-wave spectrum, while the SAR resolution is some 15 m and σ_0 is affected by the short part of the long-wave spectrum only. Waves longer than the SAR resolution cell are resolved by adjacent σ_0 .

Within the range of SAR incidence angles, tilt modulation dominates. Figure 7 displays unmodulated (dashed lines) and tilt-modulated σ_0 (full lines). The incidence angle of the upper panel is within the SAR range and, due to reduced tilt modulation, the SAR measured σ_0 fall in between the dashed and full line at the respective wind speed, i.e. the SAR underestimates the wind speed. This effect depends on the wind direction relative to the radar and is about zero at crosswind and maximum at upwind and downwind directions.

The modified σ'_0 , as seen by SAR, is related to the scatterometer (SCA) σ_0 by

$$\sigma'_0 = \sigma_0 \frac{1 + q_{\text{SAR}}}{1 + q_{\text{SCA}}} \quad (29)$$

where q is computed by means of equation (17) and σ_0 is taken from an empirical model, e.g. that of Ifremer. Considering tilt modulation only, σ'_0 depends on the second-order derivatives of the undisturbed radar cross-section, but not directly on the short-wave scattering spectrum.

The percentage underestimation of wind speed by SAR is presented in table 1. The results refer to upwind condition, i.e. the maximum deviation between SAR-retrieved and scatterometer-retrieved winds. The Ifremer model has been applied to determine both σ_0 in equation (29) and the wind speed from the modified σ'_0 . The model short-wave spectrum (equations 18–20), is used for deriving the second-order σ_0 -derivatives. However, measured spectra indicate that these values might be too high (figure 5). For this reason, calculations have been performed with derivatives reduced by a factor of 1/2. This procedure is equivalent to reducing the amplitude, i.e. the variance, of the long-wave slope spectrum by the same factor. The full long-wave spectrum is applied for calculating q_{SCA} in equation (29) and the same spectrum truncated at 15 m wavelength for q_{SAR} .

The deviation of SAR-retrieved and scatterometer-retrieved wind speed depends on the distribution of the wave-slope variance in terms of wavenumber. Strong

Table 1. Percentage underestimation of wind speed by SAR with the scatterometer σ_0 -model of Ifremer. The data refer to upwind condition ($\phi=0^\circ$) and are presented for different wind speeds U and incidence angles ϑ . Long-wave spectra used are (a) Pierson–Moskowitz, (b) JONSWAP (long fetch), (c) JONSWAP (short fetch), (d) Donelan (long fetch) and (e) Donelan (short fetch) (cf. figure 6). The values of the right-hand columns refer to the same spectra with amplitudes divided by a factor of 2. The cutoff wavenumber is 0.5 m.

U (m s^{-1})	a	b	c	d	e	a	b	c	d	e
$\vartheta=20^\circ$										
4	-2	-4	0	-3	0	-1	-2	0	-2	0
8	-19	-21	-2	-13	-1	-13	-15	-1	-11	-1
16	-20	-20	-20	-10	-9	-14	-14	-15	-9	-8
$\vartheta=23^\circ$										
4	-1	-2	0	-2	0	-1	-1	0	-1	0
8	-12	-14	-1	-9	-1	-8	-9	-1	-7	-1
16	-15	-15	-16	-8	-8	-10	-10	-11	-7	-6
$\vartheta=26^\circ$										
4	-1	-1	0	-1	0	-1	-1	0	-1	0
8	-9	-10	-1	-7	-1	-6	-6	-1	-5	0
16	-11	-11	-12	-7	-6	-7	-7	-8	-6	-5

influence can be expected if the main variance is concentrated at wavelengths longer than 15 m. Table 1 presents results, computed with the spectra of figure 6, i.e. Pierson–Moskowitz, JONSWAP and Donelan, the latter two with long and short fetch. The cutoff wavelength is 0.5 m. Considering either downwind condition or applying the CMOD4 model or considering a \cos^4 -angular dependence instead of the \cos^2 -distribution (equation 27) has only little influence on the results. A shift of the cutoff wavelength to 0.2 m, i.e. increasing the variance of shorter waves, reveals about the same values as in the right-hand columns of table 1, i.e. as those obtained by dividing the long-wave variance by 2.

In the case of wind blowing roughly towards or away from the satellite, wind speeds retrieved from SAR by means of a scatterometer σ_0 -model may underestimate the real wind. The amount of underestimation depends on the slope-spectrum of the long waves. Table 1 reveals that there is only little influence at low wind speeds (4 m s^{-1}). At higher wind speeds (8 m s^{-1}) the underestimation can exceed 10% if the fetch is long, i.e. the sea fully developed. Independent of fetch the underestimation is higher than 10% at wind speeds of 16 m s^{-1} . In addition, this effect is strongly dependent on the incidence angle.

4.2. Influence of swell on wind retrieval

Empirical scatterometer models do not account for modulation by swell, which is an occasional phenomenon and arrives from remote areas. The spectrum of the long waves may be described as a superposition of wind sea and swell. Equation (17) then yields two additive terms for the modulation of σ_0 , one accounting for wind sea, the other for swell. Distortions of the wind retrieval, caused by the presence of ocean swell, is estimated as follows. First, the modulation of the theoretical σ_0 is

determined from equation (17) by making use of swell spectra defined by

$$E_s(K) = \begin{cases} E(K) & \text{if } \Omega < \Omega_p \\ E(K) \left(\frac{K_p}{K}\right)^n & \text{otherwise} \end{cases} \quad (30)$$

where $E(K)$ is the long-wave spectra of equations (23–26), K_p is the wavenumber at the peak frequency Ω_p and n a positive integer. This approach accounts for the fact that, due to dispersion, swell arriving from remote areas is concentrated on a less broad wavenumber band than the original wind sea. Also the angle distribution is narrower, and for the numerical calculations assumed to be a δ -function:

$$S_s(\varphi) = \delta(\varphi - \varphi_s) \quad (31)$$

where φ_s is the direction of the swell relative to the mid-beam of the scatterometer, counting in accordance with the wind direction.

As a next step, the perturbation due to swell is added to the empirical σ_0 , which already accounts for the wind-sea modulation. These new values s_{0i} for the three antennas are used to retrieve wind speed and direction by minimizing the cost function of equation (3) with $K_i = 1$. The search for solutions is confined to the vicinity of the original wind vector, i.e. there is no ambiguity problem concerning the wind direction. The radar cross-sections in equation (3) refer to the three antennas which view a surface pixel under different incidence and azimuth angles. Two cases are considered, near-range with incidence angles ϑ of 18° (mid-beam) and 25° (fore-beam and aft-beam) and far-range with respective angles of 40° and 50° . The presence of swell yields deviations in both wind speed and direction.

The swell-induced modulation depends on the total variance of the slope spectrum, but not on the shape of the spectrum. Such variances are listed in table 2 for fully developed spectra, Pierson–Moskowitz, JONSWAP and Donelan (left columns), and the same spectra with increased decay at wavenumbers exceeding the peak frequency (cf. equation 30). Calculations referring to the unattenuated spectra (left-hand columns in table 2) lead to unstable results. However, it can be assumed that due to propagation effects, e.g. dispersion of the wave field and dissipation of short waves, the swell slope spectrum contains less variance than a fully developed wind sea. Considering spectra, decaying with K^{-4} or K^{-5} , i.e. $n = 1$ or $n = 2$ in equation (30), the increase of variance is small when shifting the cutoff wavenumber to smaller wavelengths than 0.5 m.

For the near-range, figure 10 displays deviations of wind direction obtained with

Table 2. Wave-slope variance (multiplied by a factor of 100) of fully developed long-wave spectra, (a) Pierson–Moskowitz, (b) JONSWAP, (c) Donelan (cf. figure 6) weighted according to equation (30) by $n = 0$ (left columns), $n = 1$ (middle columns), $n = 2$ (right columns). The cutoff wavenumber is 0.5 m.

U (m s^{-1})	a	b	c	a	b	c	a	b	c
4	1.44	1.39	2.50	0.37	0.45	0.55	0.18	0.28	0.26
8	2.13	1.98	5.43	0.38	0.46	0.60	0.18	0.28	0.26
16	2.92	2.64	11.4	0.48	0.50	0.74	0.25	0.28	0.35

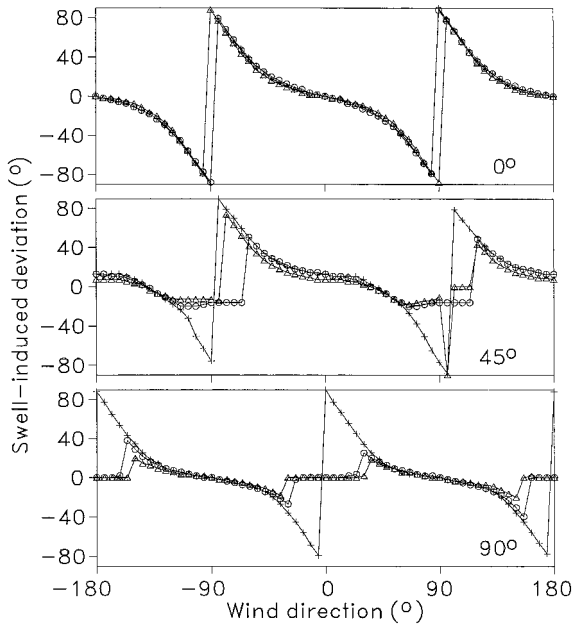


Figure 10. Swell-induced deviations of wind direction for three wind speeds U , 4 m s^{-1} (\circ), 8 m s^{-1} ($+$), 16 m s^{-1} (\triangle), in the near-range of the scatterometer (incidence angles $\vartheta = 25^\circ, 18^\circ, 25^\circ$ of for-beam, mid-beam, and aft-beam, respectively). The three panels refer to the indicated swell directions φ_s relative to the radar. The slope variance is 0.005 (cf. table 2).

a slope variance of 0.005. This variance can be realized by different long-wave spectra with $n=1$ in equation (30) (cf. table 2). Different swell directions φ_s and wind speeds U are considered. The deviations of wind speed are not shown. They are found to be positive and vary between 10 and 20% at 4 and 8 m s^{-1} wind speed and by less than 10% at 16 m s^{-1} . Figure 10 reveals maximum values of directional deviations at distinct wind directions. This behaviour is due to the formulation of the empirical σ_0 -models in terms of wind direction. The sharp peaks in figure 10 are an artifact of the δ angular distribution (equation 31).

Additional examples of the deviation of wind direction are presented in figures 11 and 12. Figure 11 refers to the near range, but as compared to figure 10 to a reduced slope variance of 0.002. The deviations of the wind direction decrease to about one-half of the values of figure 10. The same effect is found by reducing the second-order σ_0 -derivatives by a factor of 1/2, i.e. referring to the measured short wave spectrum (cf. figure 5). Figure 12 refers to the far-range and slope variance of 0.005, i.e. the same as for figure 10. Comparison of figures 10 and 12 shows that the directional deviations are larger for the near-range (small incidence angles) than for the far-range (large incidence angles). In the near-range, deviations are mainly due to tilt modulation; for the far range contributions of tilt and hydrodynamic modulation are about the same.

Nearly no influence on the angular deviations has been found when replacing the Ifremer model by CMOD4, or when introducing a Gaussian instead of the \cos^2 -dependence on wind direction in the short-wave spectrum (equations 18–20). However, inserting logarithmic σ_0 -values into the cost function (equation 3), instead

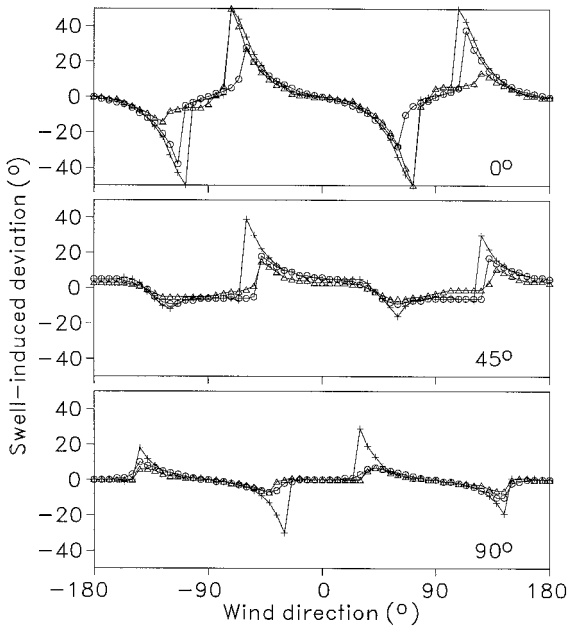


Figure 11. Swell-induced deviations of wind direction for three wind speeds U , 4 m s^{-1} (\circ), 8 m s^{-1} ($+$), 16 m s^{-1} (\triangle), in the near-range of the scatterometer (incidence angles $\vartheta = 25^\circ$, 18° , 25° of for-beam, mid-beam, and aft-beam, respectively). The three panels refer to the indicated swell directions φ_s relative to the radar. The slope variance is 0.002 (cf. table 2).

of linear ones, has some influence. The angular deviations reach about the same maximum values, but extend over larger intervals of wind direction.

5. Conclusions

By applying the composite surface scattering theory, the portion of microwave backscatter due to the modulation of long waves (wind sea) has been estimated. The investigations refer to empirical scatterometer models, derived for the C-band scatterometer of ERS-1/2, the σ_0 -models of Ifremer (1996) and CMOD4 of ESA (Stoffelen and Anderson 1997). With simple parametrizations it was possible to decompose the normalized radar cross-section σ_0 into contributions of pure ripple scattering and wind-sea modulation. Two applications are presented: (1) the underestimation of wind speed by SAR data when using scatterometer σ_0 -models; and (2) errors of retrieved wind direction when swell is present.

The composite surface scattering model used accounts for tilt and hydrodynamic modulation. The estimated portion of σ_0 due to wind-sea modulation strongly depends on the incidence angle ϑ of the radar. The contribution of tilt modulation dominates in the near-range ($\vartheta \approx 25^\circ$), in accordance with the relatively small upwind/downwind asymmetry of σ_0 as predicted by the empirical σ_0 -models, and strongly decreases with increasing ϑ . The high, but deviating, upwind/downwind asymmetries of the two σ_0 -models in the far-range ($\vartheta \approx 50^\circ$) can not be reproduced by the modulation transfer coefficient, derived by means of the principle of conservation of action. Beside shortcomings of the theoretical approach, this discrepancy may be an artifact of the selected σ_0 -model functional form. In this case, the modelled

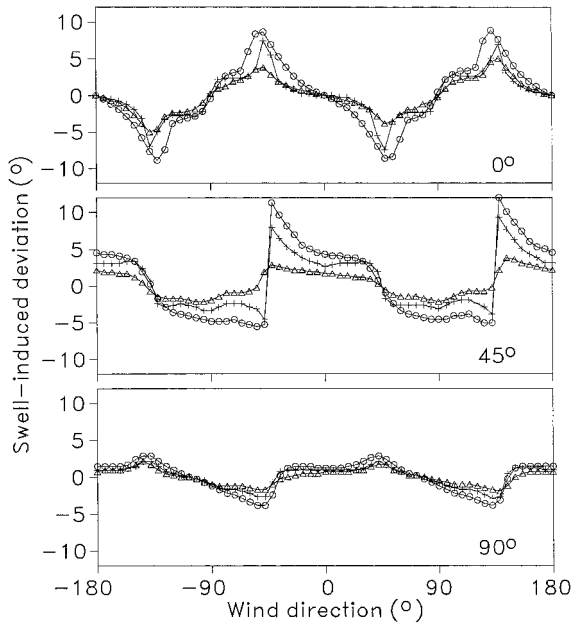


Figure 12. Swell-induced deviations of wind direction for three wind speeds U , 4 m s^{-1} (\circ), 8 m s^{-1} ($+$), 16 m s^{-1} (\triangle), in the near-range of the scatterometer (incidence angles $\vartheta = 50^\circ, 40^\circ, 50^\circ$ of for-beam, mid-beam, and aft-beam, respectively). The three panels refer to the indicated swell directions φ_s relative to the radar. The slope variance is 0.005 (cf. table 2).

modulation transfer coefficient overestimates the importance of hydrodynamic modulation. Fortunately, however, the applications presented are dominated by tilt modulation.

Both scatterometer and SAR measurements of σ_0 are performed by the AMI on ERS-1/2. However, the illuminated areas differ and in turn the influence of wind-wave modulation. Within the range of incidence angles of the ERS-1/2 SAR, tilt modulation dominates and causes an underestimate of wind speed by SAR. Tilt modulation depends on the second-order σ_0 -derivatives with respect to the facet slopes and the long-wave slope spectrum. Different methods have been used to estimate the derivatives, and different long-wave spectra have been applied for calculating the amount of underestimation. This amount depends on the wind direction and is about zero at cross-wind and maximum at upwind and downwind directions, it increases with increasing wind speed and decreases with increasing incidence angle. At wind speeds higher than some 10 m s^{-1} the underestimation can reach 20% at $\vartheta = 20^\circ$ and 12% at $\vartheta = 26^\circ$, which are the edges of the SAR beam.

The determination of the wind vector by means of an empirical σ_0 -model may be distorted by the presence of swell. Deviations of wind direction have been calculated by applying different models of the swell spectrum. A strong dependence on the incidence angle has been found. In the far range ($\vartheta \approx 50^\circ$) both tilt and hydrodynamic modulation contribute, but the calculated deviations of wind direction are below 10° , i.e. within the error bounds of 20° as assumed for ERS-1/2 wind scatterometry. Higher deviations of some 40° have been found in the near range ($\vartheta \approx 25^\circ$), where tilt modulation dominates. Dependencies on wind speed and swell

direction are rather complex. The magnitude of error depends on the slope spectrum of the swell. In general, this spectrum is not known and the estimation of swell-induced errors is impossible. However, the knowledge of dependencies of these errors on radar and environmental parameters can help to detect systematic errors in wind fields retrieved from the ERS-1/2 scatterometer. It should be mentioned that other effects than swell can introduce similar errors: for example, in coastal waters, fetch effects often mean that longer wind waves have a mean direction at a substantial angle to the wind.

Acknowledgments

The author is grateful for the suggestions of two anonymous reviewers.

References

- ALPERS, W., and HASSELMANN, K., 1978, The two-frequency technique for measuring ocean wave spectra from an airplane or satellite. *Boundary-Layer Meteorology*, **13**, 215–230.
- ALPERS, W., and STILKE, G., 1996, Observation of a nonlinear wave disturbance in the marine atmosphere by the synthetic aperture radar aboard the ERS-1 satellite. *Journal of Geophysical Research*, **101**, 6513–6525.
- DONELAN, M. A., HAMILTON, J., and HUI, W. H., 1985, Directional spectra of wind-generated waves. *Philosophical Transactions of the Royal Society of London*, **A315**, 509–562.
- DONELAN, M. A., and PIERSON, W. J. JR., 1987, Radar Scattering and equilibrium ranges in wind-generated waves with application to scatterometry. *Journal of Geophysical Research*, **92**, 4971–5029.
- HASSELMANN, K., 1971, On the mass and momentum transfer between short gravity waves and larger scale motion. *Journal of Fluid Mechanics*, **50**, 189–205.
- HASSELMANN, K., BARNETT, T. P., BOUWS, E., CARLSON, H., CARTWRIGHT, D. E., ENKE, K., EWING, J. A., GIENAPP, H., HASSELMANN, D. E., KRUSEMAN, P., MEERBURG, A., MÜLLER, P., OLBERS, D. E., RICHTER, K., SELL, W., and WALDEN, H., 1973, Measurement of wind-wave growth and swell decay during the Joint North Sea Wave Project (JONSWAP). *Ergänzungsheft zur Deutschen Hydrographischen Zeitschrift*, Series A, no. 12.
- HAUSER, D., and CAUDAL, G., 1997, Combined analysis of the radar cross-section modulation due to the long ocean waves around 14° and 34° incidence: implication for the hydrodynamic modulation. *Journal of Geophysical Research*, **101**, 25 833–25 846.
- HUGHES, B. A., 1978, The effect of internal waves on surface wind waves. *Journal of Geophysical Research*, **83**, 455–465.
- IFREMER (L'INSTITUT FRANCAIS DE RECHERCHE POUR L'EXPLOITATION DE LA MER), 1996, Off-line wind scatterometer ERS products User manual, IFREMER-CERSAT, Ref. C2-MUT-W-01-IF, Version 2.0. IFREMER, BP70, 29280 Plouzane, France.
- JANSSEN, P., and WOICESHYN, P., 1992, Wave age and the scatterometer wind retrieval algorithm. *European Space Agency workshop proceedings, ERS-1 geophysical validation, Penhors, France, 27–30 April 1992*, ESA wpp-36 (Paris: ESA), pp. 141–145.
- PIERSON, W. J., and MOSKOWITZ, L., 1964, A proposed spectral form for fully developed wind seas based on the similarity theory of S. A. Kitaigorodskii. *Journal of Geophysical Research*, **69**, 5181–5190.
- PLANT, W. J., 1986, A two-scale model of short wind-generated waves and scatterometry. *Journal of Geophysical Research*, **91**, 10 735–10 749.
- ROMEISER, R., ALPERS, W., and WISMANN, V., 1997, An improved composite surface model for the radar backscattering cross-section of the ocean surface. 1. Theory of the model and optimization/validation by scatterometer data. *Journal of Geophysical Research*, **102**, 25 237–25 250.
- RUFENACH, C., 1995, A new relationship between radar cross-section and ocean surface wind speed using ERS-1 scatterometer and buoy measurements. *International Journal of Remote Sensing*, **16**, 3629–3647.

- RUFENACH, C., 1996, An offset between scatterometer directional anisotropy and wind direction across the equatorial Pacific Ocean. *Proceedings of the International Geoscience and Remote Sensing Symposium (IGARSS'96), Lincoln, Nebraska, USA, 27–31 May 1996*, IEEE Catalog Number 96CH35876 (Piscataway, NJ: IEEE), pp. 814–816.
- SCOON, A., ROBINSON, I. S., and MEADOWS, P. J., 1996, Demonstration of an improved calibration scheme for ERS-1 SAR imagery using a scatterometer wind model. *International Journal of Remote Sensing*, **17**, 413–418.
- STOFFELEN, A., and ANDERSON, ?., 1997, Scatterometer data interpretation estimation and validation of the transfer function CMOD4. *Journal of Geophysical Research*, **102**, 5767–5780.
- STOLTE, S., 1990, Dynamik kurzweiligen Seegangs und Seegangsbrechens. Forschungsanstalt der Bundeswehr für Wasserschall und Geophysik, Forschungsbericht 1990-4, Kiel, Germany.
- ULABY, F. T., MOORE, R. K., and FUNG, A. K., 1986, *Microwave Remote Sensing, Active and Passive*, vol. III, *From theory to applications* (Washington: Artech House) 1986.
- VALENZUELA, G. P., 1978, Theories of the interaction of electromagnetic and ocean waves—a review. *Boundary Layer Meteorology*, **13**, 61–85.
- WOICESHYN, P., and JANSSEN, P., 1992, Sensitivity study—scatterometer retrievals with wave age parameter. *European Space Agency workshop proceedings, ERS-1 geophysical validation, Penhors, France, 27–30 April 1992*, ESA wpp-36 (Paris: ESA), pp. 133–139.
- WRIGHT, J. W., 1968, A new model for sea clutter. *IEEE Transactions on Antennas and Propagation*, **AP-16**, 217–223.